Published in final edited form as:
Mamm Genome. 2009 August ; 20(8): 462–475. doi:10.1007/s00335-009-9210-9.

The podosomal-adaptor protein SH3PXD2B is essential for normal postnatal development

Mao Mao[1], **Daniel R. Thedens**[2], **Bo Chang**[3], **Belinda S. Harris**[3], **Qing Yin Zheng**[3,†], **Kenneth R. Johnson**[3], **Leah Rae Donahue**[3], and **Michael G. Anderson**[1,4,*]

[1]Department of Molecular Physiology and Biophysics, The University of Iowa, Iowa City, Iowa 52242, USA

[2]Department of Radiology, The University of Iowa, Iowa City, Iowa 52242, USA

[3]The Jackson Laboratory, Bar Harbor, Maine, 04609, USA

[4]Department of Ophthalmology and Visual Sciences, The University of Iowa, Iowa City, Iowa, 52242, USA

Abstract

Podosome-type adhesions are actin based membrane protrusions involved in cell-matrix adhesion and extracellular matrix degradation. Despite growing knowledge of many proteins associated with podosome-type adhesions, much remains unknown concerning the function of podosomal proteins at the level of the whole animal. In this study, the spontaneous mouse mutant *nee* was used to identify a component of podosome-type adhesions that is essential for normal postnatal growth and development. Mice homozygous for the *nee* allele exhibited runted growth, craniofacial and skeletal abnormalities, ocular anterior segment dysgenesis, and hearing impairment. Adults also exhibited infertility and a form of lipodystrophy. Using genetic mapping and DNA sequencing, the cause of *nee* phenotypes was identified as a 1 bp deletion within the *Sh3pxd2b* gene on mouse Chromosome 11. Whereas the wild-type *Sh3pxd2b* gene is predicted to encode a protein with 1 PX domain and 4 SH3 domains, the *nee* mutation is predicted to cause a frameshift and a protein truncation altering a portion of the third SH3 domain and deleting all of the fourth SH3 domain. The SH3PXD2B protein is believed to be an important component of podosomes likely to mediate protein-protein interactions with membrane spanning metalloproteinases. Testing this directly, SH3PXD2B localized to podosomes in constitutively active *Src* transfected fibroblasts and through its last SH3 domain associated with a transmembrane member of a disintegrin and metalloproteinase family of proteins, ADAM15. These results identify SH3PXD2B as a podosomal-adaptor protein required for postnatal growth and development, particularly within physiologic contexts involving extracellular matrix regulation.

Introduction

Podosome-type adhesions (podosomes and invadopodia) are specialized adhesion structures involved in cell matrix adhesion and extracellular matrix (ECM) remodeling. Structurally, podosome-type adhesions are characterized by an actin dense core surrounded by a ring of additional proteins that drive focal membrane protrusions into surrounding tissues. Functionally, adhesion molecules and matrix metalloproteinases are enriched in podosome-

*Corresponding author: Dr. Michael G. Anderson, Department of Molecular Physiology and Biophysics, 6-430 Bowen Science Building, 51 Newton Road, Iowa City, IA 52242, (319) 335-7839 (telephone), (319) 335-7330 (FAX), michael-g-anderson@uiowa.edu.
†Current address: Department of Otolaryngology-Head and Neck Surgery, Case Western Reserve University, University Hospitals-Case Medical Center, Cleveland, OH 44106, USA.

type adhesions, allowing these finger-like protrusions to interact with and modify surrounding ECM. These features are thought to allow podosome-type adhesions to play important physiologic roles in several cell types requiring motility or ECM degradation (Linder 2007; Linder and Aepfelbacher 2003; Spinardi and Marchisio 2006; Weaver 2008).

Many protein components of the podosome-type adhesion machinery have been identified. These include actin and actin modulating proteins that form the core structure, cell adhesion receptors linking cells to ECM, proteinases mediating ECM remodeling, protein kinase transducing signals, and membrane trafficking proteins facilitating protein recruitment (Gimona and Buccione 2006; Gimona et al. 2008; Linder 2007). Amongst these proteins, two key regulators are SRC and SH3PXD2A (commonly referred to as TKS5). The tyrosinase kinase SRC is a key molecule for inducing podosome-type adhesions (Destaing et al. 2008; Gimona et al. 2008). SH3PXD2A is a substrate of SRC (Lock et al. 1998) and has been described as a major organizer of podosome-type adhesions by multiple groups (Courtneidge et al. 2005; Oikawa et al. 2008; Symons 2008; Thompson et al. 2008). Upon SRC activation SH3PXD2A is recruited to the plasma membrane through interactions with PtdIns(3,4)P_2, which is enriched in podosomes (Abram et al. 2003; Oikawa et al. 2008). Recruitment of SH3PXD2A subsequently recruits other molecules such as WAS and WASL (commonly referred to as WASp and N-WASp, respectively), which stimulate ARP 2/3 complex-mediated actin nucleation and podosome extension (Oikawa et al. 2008). Recently, a homolog of SH3PXD2A, SH3PXD2B, has been identified and shown to also influence podosomes of cells in culture (Buschman et al. 2009; Courtneidge et al. 2005). Although identification of SH3PXD2A and SH3PXD2B in cells in culture suggests that these adaptor proteins are likely to play determinative roles influencing behavior of podosome-type adhesions, much remains unknown concerning the function of these proteins within the physiological context of the whole animal.

Here, we present identification and mutant phenotypes associated with a unique spontaneously arising allele of *Sh3pxd2b* in mice. Mice homozygous for the *nee* mutation exhibit runted growth and striking developmental abnormalities of several mesenchymal derived tissues, including craniofacial structures, the ocular irideocorneal angle, and white adipose tissue. Through genetic crosses designed to identify the basis of the *nee* mutation, we demonstrate a 1 bp deletion in the *Sh3pxd2b* gene. Based on sequence homology, the *Sh3pxd2b* gene is predicted to encode an adaptor protein with homology to SH3PXD2A, a key regulator of podosome-type adhesions. Testing the hypothesis that the SH3PXD2B protein is indeed a podosomal-adaptor protein, we demonstrate here that SH3PXD2B also localizes to podosomes, and as expected for an adaptor protein, is capable of binding transmembrane metalloproteinases such as ADAM15. Combined, these data support a role for SH3PXD2B as a podosomal-adaptor protein and implicate podosomes as important biological regulators of mammalian postnatal growth and development.

Materials and methods

Animal husbandry

All mice were obtained from The Jackson Laboratory, Bar Harbor, Maine. Mice were subsequently housed and bred at the University of Iowa Research Animal Facility. The spontaneous *nee* mutation arose in strain B10.A-*H2*^{h4}/(4R)SgDvEg at generation F51 and subsequently was maintained by the Mouse Mutant Resource of The Jackson Laboratory (http://mousemutant.jax.org/index.html). Since both male and female homozygotes are infertile, the strain was maintained by progeny testing or ovarian transplantation. In the past, the mutation has also been referred to as *nm2702* (Chang et al. 2005). With advice of The Mouse Genomic Nomenclature Committee, the mutation will here after be referred to as *nee* to indicate phenotypic defects associated with the mutation (nose, eye, ear). Upon molecular

identification of the mutation, mice were genotyped by assaying the absence or presence of an *RsaI* restriction enzyme site abolished by the *nee* mutation and the stock maintained in heterozygote X heterozygote crosses. Mice were maintained on a 4% fat NIH 31 diet provided *ad libitum* and were housed in cages containing dry bedding (Cellu-dri; Shepherd Specialty Papers, Kalamazoo, MI). The environment was kept at 21°C with a 12-hour light: 12-hour dark cycle. All animals were treated in accordance with the Association for Research in Vision and Ophthalmology Statement for the Use of Animals in Ophthalmic and Vision Research. All experimental protocols were approved by the Animal Care and Use Committee of The University of Iowa or The Jackson Laboratory.

Craniofacial assessment

Craniofacial measurements were made for mutants and controls on skulls prepared by incomplete maceration in potassium hydroxide, stained with alizarin red, and stored in undiluted glycerin (Green 1952). A set of 7 standard skull measurements were collected using digital hand calipers (Stoelting, Wood Dale, IL). Landmarks were adapted from those used by Dr. Joan Richtsmeier to characterize craniofacial morphology in mouse models of Down Syndrome (Richtsmeier et al. 2000) and have been validated for accuracy and precision by the Craniofacial Resource at The Jackson Laboratory (http://craniofacial.jax.org/).

Slit-lamp examination

Anterior chamber phenotypes were assessed with a slit-lamp (SL-D7; Topcon, Tokyo, Japan) and photodocumented with a digital camera (D100; Nikon, Tokyo, Japan). Images were taken with identical camera settings and prepared with identical image software processing.

Magnetic resonance and X-ray imaging

Imaging of adipose tissue by magnetic resonance imaging (MRI) was performed on a 4.7 Tesla Varian Unity/INOVA small-bore MRI system (Varian Inc., Palo Alto, CA). After anesthesia with isoflurane, T1-weighted images were acquired in the coronal plane using a fast spin-echo pulse sequence with TR/TE = 600/12 ms, an echo train length of 2, and 4 averages. A matrix size of 512 × 128 covered a field of view of 60–90 mm × 30 mm with 15 slices of 1.1–1.5 mm thickness separated by a 0.2–0.5 mm gap depending on the size of the animal. Imaging of skeletal morphology by X-ray was performed with euthanized mice and a Faxitron MX20 Specimen X-ray system (Faxitron X-Ray LLC, Lincolnshire, IL) using 25 kV 1 min exposures on Kodak Portal Pack Oncology X-ray film.

Auditory-evoked brain stem response analysis and ear histology

Auditory-evoked brain stem response (ABR) threshold analysis was performed using previously described methods (Zheng et al. 1999). Briefly, mice anesthetized with tribromoethanol were presented with broad-band click and pure tone 8-, 16-, and 32-kHz stimuli at intensities varying between 10 and 100 dB SPL (decibels sound pressure level), and the evoked brain stem responses were recorded. Auditory thresholds were obtained for each stimulus by varying the SPL at 5-dB steps to identify the lowest level at which an ABR pattern can be recognized. Inner and middle ears were dissected from the skull following perfusion with Bouin's fixative. Tissues were decalcified in Bouin's fixative for 14 days and embedded in paraffin. Cross sections were cut at 7 μm, mounted on glass slides, and stained with hematoxylin/eosin.

Measurement of body composition and bone mineral density

Areal bone mineral density of the whole body and percent fat body mass were determined on mice anesthetized by intraperitoneal injection with Avertin (tribromoethanol stabilized in tertiary amyl hydrate), 1 mg per 2 g of body weight. Data were collected using a PIXImus small

animal dual-energy X-ray absorptiometry (DEXA) densitometer (GE Healthcare, Waukesha, WI), reconfigured with lower X-ray energy than in human DEXA machines in order to achieve contrast in small specimens, and utilizing manufacturer supplied software (Lunar PIXImus version 1.46). Resolution of the PIXImus is 0.18 × 0.18 mm pixels with a usable scanning area of 80 × 65 mm. Calibration and daily quality assurance was achieved using a phantom with known values.

Gene mapping and sequencing

To determine the chromosomal location of the *nee* mutation, B10.A-*H2*^{h4}/(4R)SgDvEg-*nee* mice were mated with CAST/EiJ mice and the F1 mice, which exhibited no visible abnormalities, were intercrossed to produce F2 mice. Genomic DNA of 45 affected F2 progeny was prepared as previously described (Buffone and Darlington 1985) and genotyped by analyzing polymorphic microsatellite markers by agarose electrophoresis, utilizing standard conditions and protocols. The initial genome scan was carried out on pooled DNA samples. After detection of linkage on Chr 11, microsatellite markers *D11Mit295, D11Mit19, D11Mit152, D11Mit215* and *D11Mit186* were scored on individual DNA samples. Candidate genes localized to the critical region between markers *D11Mit19* and *D11Mit186* were identified by scanning the Ensembl genome database (Release 53). Following PCR amplification of exons of interest from genomic DNA isolated from either the mutant B10.A-*H2*^{h4}/(4R)SgDvEg-*nee* or wild-type parental B10.A-*H2*^{h4}/(4R)SgDvEg strain, products were purified (QIAquick PCR Purification Kit; Qiagen, Inc., Valencia, CA), sequenced by automated fluorescence tagged sequencing, and directly compared to each other. Confirmation of the *nee* mutation was performed by PCR amplification of a 713 bp DNA fragment flanking the deleted adenine residue (using primers: forward: 5' AGGCTCAGTTGCCCTGAATGTA 3'; reverse: 5' TTCTCAGCGGGAACTTGCTCTT 3') from various strains of mice and digestion of the amplicons with *Rsa*I. DNA containing the *nee* allele is predicted to be resistant to cleavage, while wild-type alleles are predicted to give rise to products of 546 bp and 167 bp. Numeration for the *Sh3pxd2b* mRNA is based on NCBI RefSeq NM_177364.3.

Preparation of anti-SH3PXD2B antiserum

Constructs generating GST-fused SH3PXD2B were generated by PCR-assisted cloning. To reduce the possibility for cross reaction with the closely related SH3PXD2A protein, the antibody was raised against a region between the third and fourth SH3 domains of SH3PXD2B having low identity with SH3PXD2A. Using oligonucleotides specific to a portion of *Sh3pxd2b* exon 13 (encoding amino acids 440–751) and genomic DNA of C57BL/6J mice as template, the resulting amplification product was first cloned into a TA cloning vector (pCR2.1-TOPO vector; Invitrogen, Carlsbad, CA) and then subcloned into a GST gene fusion vector (pGEX6p-1; GE Healthcare, Piscataway, NJ). Correct fusion of this construct was confirmed by automated fluorescence tagged sequencing. Following transformation into the BL21 (DE3) strain of *Escherichia coli*, protein expression was induced and cell lysates collected. GST-fused protein was first purified using a glutathione-Sepharose 4B column followed by excision of GST from the protein (PreScission protease; GE Healthcare, Piscataway, NJ). SH3PXD2B-specific antiserum was generated in rabbits and affinity purified (Sigma-Genosys; The Woodlands, TX).

Construction of plasmids encoding GFP-SH3PXD2B

Plasmids encoding GFP-fused full-length SH3PXD2B (GFP-SH3PXD2B) were constructed by PCR-assisted cloning. DNA fragments containing wild-type *Sh3pxd2b* were amplified by RT-PCR from total RNA extracted from eyes of C57BL/6J mice. The resulting fragments were first cloned into an entry vector (pCR8/GW/TOPO; Invitrogen, Carlsbad, CA) and then subcloned by LR recombination into an expression vector containing an N-terminus GFP tag

(pcDNA-DEST53; Invitrogen, Carlsbad, CA). Plasmids encoding GFP-fused mutant SH3PXD2B with the 1303A deletion (GFP-SH3PXD2B^{1303delA}) were constructed by PCR based site-directed mutagenesis using the wild type construct as a template. Sequences of both plasmid inserts were confirmed by automated fluorescence tagged sequencing.

Cell culture and transfection

Cells were maintained at 37°C in a humidified atmosphere containing 5% CO_2. HEK 293T and mouse NIH3T3 cells were cultured in DMEM supplemented with 10% FBS, 100 units/ml penicillin, and 100 units/ml streptomycin. Formation of podosomes was induced by transient transfection of a previously described constitutively active *Src* (Y529F) construct (Sharma et al. 2007). Transfections utilized the Lipofectamine 2000 transfection reagent (Invitrogen, Carlsbad, CA) with additional use of the PLUS Reagent enhancing agent (Invitrogen, Carlsbad, CA) in NIH3T3 cells, following the manufacturer's recommended protocols.

Immunofluorescence and microscopy

Cells cultured on coverslips were fixed in 4% paraformaldehyde in PBS for 10 min and incubated in permeabilization buffer (0.1M glycine, 0.05% Triton X-100 in PBS) containing 3% BSA for 30 min. Following permeabilization, cells were blocked with permeabilization buffer containing 15% goat serum and 3% BSA for 15 min. Fixed cells were incubated with anti-SH3PXD2B antibody for 1 hr (1:200 dilution in permeabilization buffer with 1% BSA and 1% goat serum), washed with PBS, and incubated with a 1:200 dilution of secondary antibody and 1:100 dilution of phalloidin (Alexa633-conjugated goat anti-rabbit and Alexa546-phalloidin; Invitrogen, Carlsbad, CA). After mounting (ProlongGold; Invitrogen, Carlsbad, CA), cells were imaged with a confocal microscope (Zeiss LCM 510; Carl Zeiss MicroImaging, Inc., Thornwood, NY). Cells transfected with GFP-fusion plasmids were fixed with 4% paraformaldehyde in PBS for 10 min; following washes, cells were mounted and imaged as described above.

GST pull-down assay

GST and a GST-fusion containing the fourth SH3 domain spanning amino acids 842–908 of SH3PXD2B (GST-SH3#4) were expressed in BL21 (DE3) cells and purified using a glutathione-Sepharose 4B column (GE Healthcare, Piscataway, NJ). Cell lysates (50 μg) were incubated with glutathione-Sepharose 4B beads for 2 h at 4°C, washed, and then blocked in EB buffer (10 mM Tris-HCl pH 7.4, 50 mM NaCl, 1% Triton X-100, 50 mM NaF, 0.1% BSA, 2 mM Na_3VO_4) supplemented with an additional 5% BSA at 4°C overnight. HEK 293T cells expressing MYC-tagged full length ADAM15 were generated using PCR to amplify the *Adam15* cDNA followed by cloning with gateway technology into an expression vector (pcDNA-DEST53; Invitrogen, Carlsbad, CA). 293T cells transfected with *Adam15-myc* plasmid were lysed 48 h after transfection in EB buffer supplemented with 1 mM PMSF and a mix of additional protease inhibitors (Complete Mini Protease Inhibitor Cocktail; Roche Applied Science, Indianapolis, IN). Cell debris was removed by centrifuging at 12,000 rpm for 10 min. GST-fusion coated beads were washed 3 times with EB buffer and incubated with 1 mg total cell lysates for 2 hours at 4°C. Following 6 washes with EB buffer, beads were recovered by centrifugation and dissolved in Laemmli buffer. Bound protein was analyzed by 7.5% SDS-PAGE and immunoblotting. Blots were blocked with 10% BSA in TBST (Tris-buffered saline with 0.1% Tween-20) followed by antibody incubations and washes in TBST using 1:1000 dilution of anti-c-MYC rabbit polyclonal antibody (Novus Biologicals, Littleton, CO) and 1:4000 dilution of horseradish peroxidase conjugated goat anti-rabbit IgG (Invitrogen, Carlsbad, CA). Immunoreactivity was detected by enhanced chemiluminescence methodology (GE Healthcare, Piscataway, NJ).

Tissue expression analysis

Protein levels of SH3PXD2B in various tissues were analyzed with western blot. Tissues dissected from a mouse from the *nee* colony homozygous for wild-type *Sh3pxd2b* alleles were minced and homogenized with a rotor/stator tissue homogenizer in cell lysis buffer (50mM Tris-HCl pH 7.4, 150mM NaCl, 1mM EDTA, 0.1% Triton X-100, 0.1% SDS) supplemented with 1 mM PMSF and a mix of additional protease inhibitors (Halt Proteinase Inhibitor Cocktail; Thermo Scientific, Rockford, IL). Total tissue lysates were centrifuged at 14,000 rpm for 20 min at 4°C. Protein concentration in the resulting supernatant was determined using the BCA protein assay reagent (Sigma-Aldrich, St Louis, MO). Using 50 μg of lysate per lane, protein from each tissue was electrophoresed on 7.5% SDS-PAGE gels and transferred to membranes (Immobilon-FL membrane; Millipore, Bedford, MA). Membranes were blocked for 1 h at room temperature in Odyssey Blocking Buffer (LI-COR Biosciences, Lincoln, NE) diluted 1:1 in PBS. All antibody incubations were performed using a 1:1 solution of Odyssey Blocking Buffer and PBS supplemented with 0.2% Tween-20. Primary antibody was incubated with membranes at 4°C overnight using a 1:2000 dilution of anti-SH3PXD2B rabbit polyclonal antibody. As a control for protein transfer, membranes were similarly incubated with 1:1000 dilution of anti-β-actin rabbit polyclonal antibody (Sigma-Aldrich, St Louis, MO). After washes with PBS, membranes were incubated for 1 h at room temperature with secondary antibody diluted 1:2000 (IRDye680 goat anti-rabbit IgG; LI-COR Biosciences, Lincoln, NE) and visualized with an infrared scanner (Odyssey Infrared Imaging System; LI-COR Biosciences, Lincoln, NE).

Results

The spontaneous *nee* mutation causes growth, craniofacial, ocular, and ear defects

Following a phenotype-driven approach for identifying new mouse models of human disease, the *nee* mutation is a spontaneously arising mutation that was initially identified by the Mouse Mutant Resource of The Jackson Laboratory. Mice homozygous for the *nee* mutation were initially recognized because of their small body size, abnormal craniofacial morphology, and ocular defects (Fig. 1).

The most obvious defect of *nee* homozygotes was their small body size (Fig. 1a, b). At birth, *nee* homozygotes were visibly indistinguishable from wild-type mice. By 2 months of age, *nee* homozygotes were dramatically smaller in body weight (10.2 ± 1.5 g; mean ± SD; $n = 4$) compared to either heterozygote (18.8 ± 0.7 g; $n = 9$) or wild-type (18.0 ± 1.9 g; $n = 5$) littermates ($P < 0.004$ in both comparisons, Student's *t*-test). Subsequent to 2 months of age, while heterozygous and wild-type mice both continued to grow in body weight, mice homozygous for the *nee* mutation did not. As heterozygous and wild-type mice reached normal adult weights by 6–12 months of age (28.3 ± 5.1 g; $n = 11$ and 28.0 ± 7.9 g; $n = 5$; respectively), *nee* homozygotes remained runted at both the 3–5 month (10.9 ± 1.9 g; $n = 8$) and 6–12 month (11.7 ± 2.7 g; $n = 7$) age periods. As a consequence, the difference in body weight among adult mice was highly significant ($P < 0.0007$ comparing homozygotes to heterozygotes or wild-type littermates, 6–12 month old mice, Student's *t*-test).

Two additional externally visible phenotypes were initially appreciated in *nee* homozygotes. All *nee* homozygotes have craniofacial and ocular abnormalities. Compared to control mice, all *nee* homozygotes had shortened noses (nose length: skull length = 0.629; heterozygous littermates = 0.687) and domed skulls (skull length: skull width = 1.750; heterozygous littermates = 2.141; $n = 12$ mice per group; $P < 0.0001$; Student's *t*-test) (Fig. 1c, d). Also, eyes of all *nee* homozygotes had abnormalities (Fig. 1e – h), typically appearing bulging with white corneal opacities. Examined by ophthalmic slit-lamp, corneal opacities of varying severity were confirmed in all eyes of *nee* homozygotes ($n = 14$ mice, 1–8 months in age), whereas

corneal opacities were rare in eyes of age-matched controls (a single corneal opacity was observed from all mice examined; $n = 12$ heterozygous littermate controls, 11 wild-type littermate controls). Where unobstructed views of the anterior chamber were possible in *nee* homozygotes, peripheral anterior synechia were always observed and the anterior chamber depth was increased. Combined, these clinical observations indicated that *nee* homozygotes have a developmental anterior segment dysgenesis.

In addition to the externally visible phenotypes of *nee* homozygotes described above, several other phenotypes were also discovered. First, both male and female homozygotes were infertile. Fertility could be restored by ovarian transplants of ovaries from homozygotes to wild-type mice and mating to heterozygous males, indicating that the reason for female infertility did not reside in the ovary but elsewhere in the female reproductive tract. Second, *nee* homozygotes had multiple skeletal abnormalities (Fig. 2). Examination of skeletal structures by radiographic analysis indicated that *nee* homozygotes have a proportionally smaller skeleton (Fig. 2a) and abnormalities of the skull (Fig. 2b, c). Radiography of the skull from *nee* homozygotes again indicated a reduced length along the anterior-posterior axis. Higher magnification images of the hind leg (Fig. 2d, e) showed reduced dimensions, but otherwise normal gross anatomy. Both the skull and hind leg of *nee* homozygotes exhibited decreased radio-opacity, suggesting a potential decrease in bone density. To test this quantitatively, DEXA analyses were performed. In comparison to sex-matched heterozygous littermates, 12-week-old *nee* homozygotes exhibited reduced areal bone mineral density (aBMD). This difference was present in both males (*nee* homozygotes, 0.035 g/cm^2; heterozygous littermates, 0.048 g/cm^2) and females (*nee* homozygotes 0.031 g/cm^2; heterozygous littermates, 0.049 g/cm^2) and was statistically significant ($n = 6$ mice per sex per genotype; $P < 0.0001$; Student's *t*-test). Female homozygotes had significantly lower aBMD than male homozygotes ($P < 0.001$; Student's *t*-test); there was no sex difference in heterozygotes. Third, mice homozygous for *nee* have hearing impairment and middle ear pathology (Fig. 3). ABR measurements revealed that *nee* mice have elevated thresholds to broad-band click and 8 kHz, 16 kHz, and 32 kHz pure tone stimuli (Fig. 3a). Hearing impairment was neither progressive nor frequency dependent, as elevated ABR thresholds (40–50 dB above normal) were found in all four stimuli at all ages tested ($n = 13$ *nee* homozygotes and 3 heterozygous control mice; 34–92 days of age). Histological analysis further revealed that hearing impairment in these mice was likely due to middle ear inflammation (otitis media, Fig. 3b, c). Serous fluid with diffuse neutrophils was found in the middle ear cavities of all *nee* homozygotes examined, but not in control mice ($n = 6$ *nee* homozygotes and 3 heterozygous control mice), and the surrounding epithelium was markedly thickened by fibrous connective tissue and embedded neutrophils. No other structural abnormalities were observed. Similar results have previously been observed; mice with craniofacial abnormalities that include middle ear cavity or Eustachian tube dysmorphologies often develop otitis media (Zheng et al. 2006). Together, these results indicate that *nee*-mediated hearing deficiency is likely a secondary consequence of the craniofacial abnormalities of *nee* homozygotes, which presumably render the middle ear sensitive to infection. Finally, *nee* homozygotes developed a form of lipodystrophy (Fig. 4). Initially noted in dissections (Fig. 4a, b), and subsequently confirmed with MRI (Fig. 4c – h), adult *nee* homozygotes had severely depleted visceral and subcutaneous white adipose tissue ($n = 3$ mice examined, 6–11 months in age). In contrast, residual interscapular brown adipose tissue was still present. Adipose defects were less striking in young mice. While adipose defects were not observable by MRI in young mice, DEXA analyses showed a subtle reduction in percent body fat in 12-week-old *nee* homozygotes compared to heterozygous littermate controls (14% vs 19% respectively, $n = 20$ mice per group; $P < 0.001$; Student's *t*-test). With the exception of aBMD, no other sex-specific differences were observed in any phenotypes of *nee* mice. Aside from the above mentioned defects, *nee* homozygotes were otherwise relatively healthy, with many mice living to at least 12 months of age.

The *nee* mutation maps as a recessive factor to Chr 11

In order to identify the molecular basis of the *nee* mutation, an intersubspecific intercross between CAST/EiJ and *nee* mice was performed (Fig. 5). Whereas on the B10.A-*H2*^{h4}/(4R) SgDvEg genetic background, the *nee* mutation was fully penetrant and close to the expected 25% of affected progeny were produced in heterozygous matings (60 mutants / 300 total mice born = 20%), heterozygotes from the intercross with CAST/EiJ produced lower than the expected number of mutants in the F2 generation (27 mutants / 224 total mice born = 12%) and of the mice born, 5% of homozygotes died before weaning. Linkage analysis revealed that *nee* segregates as a simple recessive factor. Haplotype analysis based on 45 F2 affected mice mapped the mutation to a region on Chr 11 (Fig. 5a). The minimal critical region defining the *nee* interval was delimited proximally by marker *D11Mit19* and distally by marker *D11Mit186*, spanning a 9.7 Mb region.

The *nee* mutation is caused by a 1 bp deletion in *Sh3pxd2b*

According to the Ensembl genome database, the *nee* critical region included a total of 65 protein coding genes encompassed by 718 exons. A sequence-driven approach was utilized to identify the mutation. Based on previously described phenotypes of targeted mutations in mice, several genes in the interval were initially considered reasonable candidates, including *Fgf18* and *Npm1* (Grisendi et al. 2005; Ohbayashi et al. 2002). However, sequencing of all known exons from these candidates failed to detect any changes. In continuing analysis of the region, a total of 225 different exons divided among multiple genes were analyzed. From these, the *nee* mutation was identified as a 1 bp deletion in the last exon of *Sh3pxd2b* at nucleotide position 1303 of the predicted mRNA (Fig. 5b). The 1303delA change was the only change detected and was confirmed by independent amplification and sequencing of two additional affected mice (data not shown).

To stringently confirm the status of the 1303delA alteration as a unique mutation, a restriction enzyme based assay distinguishing this allele was designed. The 1303delA deletion disrupts an *Rsa*I restriction site. Therefore, DNA containing the wild-type allele should be sensitive to *Rsa*I digestion while *nee* DNA should be resistant. Using this assay, 10 phenotypically normal inbred mouse strains were examined for the potential presence of the *nee* allele (Fig. 5c). Resistance to *Rsa*I digestion was present only in *nee* DNA and not in DNA from other phenotypically normal strains, confirming that the 1 bp deletion in *Sh3pxd2b* was unique and highly likely to be the mutation of *nee* mice.

The *Sh3pxd2b* gene is predicted to encode a 908 amino acid protein with an N-terminus PX domain and four SH3 domains (Fig. 5d). The 1303delA deletion is predicted to cause a frameshift altering 37 amino acids before causing a premature stop codon and protein truncation altering a portion of the third SH3 domain and completely deleting the fourth SH3 domain (Fig. 5d). To investigate the potential influence of the1303delA deletion on localization of the SH3PXD2B protein, GFP fusion constructs encoding the wild-type (GFP-SH3PXD2B) and mutant proteins (GFP-SH3PXD2B^{1303delA}) were transfected into HEK 293T cells (Fig. 6). As previously observed by others (Hishida et al. 2008), the absence or presence of SH3 domains in SH3PXD2B influenced localization. Whereas wild-type SH3PXD2B was restricted to the cytoplasm (Fig. 6a), the mutant protein was present throughout the cell, including prominent localization within the nucleus (Fig. 6b). Thus, the *Sh3pxd2b*^{nee} mutation is predicted to encode a truncated protein, which as a consequence of the mutation, likely has altered subcellular distribution.

SH3PXD2B is a widely expressed podosomal-adaptor protein

The SH3PXD2B protein, and the closely-related SH3PXD2A, have both been demonstrated in cell culture studies to function as adaptor proteins required for formation of podosomes

(Abram et al. 2003; Buschman et al. 2009; Courtneidge et al. 2005). The PX domains of both SH3PXD2B and SH3PXD2A bind to the lipids PtdIns(3)P and PtdIns(3,4)P_2 while their SH3 domains bind and influence various matrix metalloproteinases and ADAM family proteinases (Abram et al. 2003; Buschman et al. 2009). Through these interactions, SH3PXD2A and SH3PXD2B are thought to tether and regulate the localization of ECM modifying enzymes to precise cellular compartments such as podosomes. To further test how the *Sh3pxd2b*^{nee} mutation might influence podosomes important to murine postnatal growth and development, we next tested whether SH3PXD2B localizes to podosomes and whether the deleted SH3 domain was capable of mediating a protein-protein interaction with a candidate protein, ADAM15 (Fig. 7).

Properties of podosomes have been well described in *Src* transformed fibroblasts (Tarone et al. 1985). To test whether SH3PXD2B localizes to podosomes in these cells, NIH3T3 cells were transfected with a constitutively active form of *Src* (Y529F) and localization of endogenous SH3PXD2B tested with an anti-SH3PXD2B specific antibody (Fig. 7a – c). While SH3PXD2B localized to the cytoplasm in untransfected cells (data not shown), a portion of SH3PXD2B localized to podosome clusters and rosettes in *Src* (Y529F) transfected fibroblasts. Consistent with other recent findings (Buschman et al. 2009), this result independently confirms that SH3PXD2B localizes to podosomes.

Although direct protein binding partners for SH3PXD2B have not previously been described, several interactions for the closely related SH3PXD2A protein are known. It has previously been demonstrated by *in vitro* binding assays that SH3PXD2A can form protein-protein interactions with ADAM family proteins, including ADAM12, ADAM15, and ADAM19. These interactions are mediated by multiple PxxP motifs present within the cytoplasmic tail of ADAMs and the fifth SH3 domain of SH3PXD2A (Abram et al. 2003). Because the fifth SH3 domain of SH3PXD2A has homology to the fourth SH3 domain of SH3PXD2B (55% identity), we reasoned that the proteins may have similar binding partners. To test this, a GST pull-down experiment was performed with a candidate of interest, ADAM15 (Fig. 7d). A fusion protein containing the fourth SH3 domain of SH3PXD2B was incubated with lysates of 293T cells transfected with a MYC-tagged full-length ADAM15. While negative controls containing GST alone did not interact with ADAM15, the fusion protein containing the fourth SH3 domain of SH3PXD2B did. This result is consistent with a role of SH3PXD2B as an adaptor protein. Furthermore, because the mutant *Sh3pxd2b*^{nee} allele is predicted to encode a protein in which all of this fourth SH3 domain is absent, this result suggests that misregulation of ADAM15 likely contributes to mutant phenotypes of *nee* mice.

In order to further relate functions of SH3PXD2B to the mutant phenotypes of *nee* mice, western blot analysis was utilized to determine the tissue distribution and levels of SH3PXD2B in wild-type mice (Fig. 7e). A band of 120 kDa was detected in protein lysates isolated from tissues of adult wild-type mice. Presumably a consequence of post-translational modifications, the apparent molecular weight of SH3PXD2B shown on SDS-PAGE gel was slightly larger than predicted (102 kDa). Because the anti-SH3PXD2B antibody was generated against a portion of the SH3PXD2B protein deleted by the *nee* mutation, it was not possible to test levels or localization of the mutant protein. However, wild-type SH3PXD2B was present in the majority of tissues, including eye, white adipose tissue, brown adipose tissue, lung, heart, brain, spleen, stomach, liver, and skeletal muscle. No protein was detected in the kidney or bone marrow, indicating that the protein is not ubiquitously expressed. With the exception of lung and skeletal muscle tissue, the relative amount of protein in each tissue resembled previously reported *Sh3pxd2b* mRNA levels in these tissues (Buschman et al. 2009;Hishida et al. 2008).

Discussion

Phenotype-driven genetics is a powerful approach for studying genetic pathways important to human health and disease. One advantage of this approach is that it often gives rise to animal models with a diversity of mutant alleles and genetic backgrounds. Here, we have utilized the *nee* mutation, which spontaneously arose on a B10.A-*H2*^{h4}/(4R)SgDvEg genetic background, to link functions of the *Sh3pxd2b* gene with multiple defects of postnatal growth and development. Initially recognized because of runted growth, craniofacial abnormalities, and ocular anterior segment dysgenesis recognizable from an early age, we have also found that adult mice homozygous for the *nee* mutation exhibit infertility, hearing deficiency, reduced areal bone mineral density, and a form of lipodystrophy depleting white adipose tissue. Mapping of the causative mutation led to identification of a protein truncating mutation in *Sh3pxd2b*, a gene about which relatively little is known (Buschman et al. 2009; Courtneidge et al. 2005; Hishida et al. 2008). Based on previous work (Buschman et al. 2009), and our own direct data presented here, *Sh3pxd2b* encodes a widely expressed podosomal-adaptor protein. In nearly all of the tissues affected by the *Sh3pxd2b*^{nee} mutation, podosomes have previously been observed and implicated in functional contributions. Combined, these data add to the mounting evidence linking roles for podosomes in multiple physiological contexts involving ECM regulation.

Role of podosomes in *nee* affected tissues

Podosomes and ECM remodeling are both known to play significant roles in bone biology (Krane and Inada 2008; Ory et al. 2008; Saltel et al. 2008). Podosomes have been particularly well studied in osteoclasts, a specialized cell that digests bone matrix in a process involving formation of podosomes. Growth retardation and craniofacial defects have previously been noted in mice with mutations influencing osteoclast function (Chen et al. 2007; Holmbeck et al. 1999; Kornak et al. 2001; Shi et al. 2008). As would be expected for a podosomal-protein influencing osteoclasts, mutations in *Src* result in growth retardation, craniofacial defects, and osteopetrosis (Soriano et al. 1991). Interestingly, mutations in other genes linked to podosomes, such as genes encoding various metalloproteinases, can lead to decreases in bone mineral density (Egeblad et al. 2007; Holmbeck et al. 1999; Mosig et al. 2007). Our observation of decreased areal bone density in *nee* homozygotes suggests that *Sh3pxd2b* is an important member of this later type of genetic pathway influencing skeletal and craniofacial development.

In the eye, podosome-like structures have been observed in trabecular meshwork cells. When cultured on a layer of collagen, these cells exhibit focal degradations of collagen overlapping spots of podosome-like structures (Aga et al. 2008). The trabecular meshwork is an ECM-rich filter for aqueous humor outflow located in the irideocorneal angle. Trabecular meshwork defects can cause elevated intraocular pressure and likely contribute to human glaucoma (Acott and Kelley 2008). From the constellation of ocular phenotypes we have observed, it is likely that developmental malformation of the irideocorneal angle or inefficient ECM remodeling mediated by a disruption of podosomes results in elevated intraocular pressure (causing increased depth of the anterior chamber) and damaging the corneal endothelium (causing corneal opacities). Given these observations, it is possible that *nee* homozygotes may also develop glaucoma, a hypothesis we are currently testing directly.

There are also links between podosomes and fertility. In males, the tubulobulbar complex, a type of intercellular junction important in sperm release and spermatocyte translocation, is thought to have properties resembling podosomes (Young et al. 2009a; Young et al. 2009b). Thus, SH3PXD2B may influence male fertility through function of these structures. Another distinct possibility is that SH3PXD2B might contribute to fertility via regulation of ADAMs (Eto et al. 2002; Evans 2001). ADAM15, the protein we have shown may interact with SH3PXD2B through its last SH3 domain, is present in mouse spermatozoa (Pasten-Hidalgo et

al. 2008) and binds effectively to oocytes (Eto et al. 2002). Thus, the infertility of *nee* mice may also be a consequence of ADAM15 mislocalization. In females, potential links to podosomes are less clear, but it is noteworthy that defects in the female reproductive tract have previously been observed in mice with targeted mutations of other genes associated with podosomes (Holmbeck et al. 1999; Shimizu et al. 2005).

Podosomes have not previously been reported in adipose tissue, but may well exist. Aside from our observation that mice homozygous for the *nee* mutation develop a form of lipodystrophy, a role for SH3PXD2B in adipose tissue has recently been independently reported in differentiation of 3T3-L1 preadipocyte cells (Hishida et al. 2008). Based on the finding that *Sh3pxd2b* was expressed early in the differentiation process of 3T3-L1 preadipocytes, Hishida et al. performed RNAi-mediated knockdown experiments and found that *Sh3pxd2b* function is required for preadipocyte differentiation and clonal expansion. Interestingly, adipocyte differentiation is also influenced by multiple proteases, including MMP14 (MT1-MMP), MMP2, and MMP9 (Bourlier et al. 2005; Chun et al. 2006).

In addition to influencing podosomes, an alternative hypothesis is that SH3PXD2B may regulate metalloproteinases with sheddase activity. For example, MMP14 (MT1-MMP) negatively regulates osteoclastogenesis by causing ectodomain shedding of TNFSF11 (RANKL) (Hikita et al. 2006). It is therefore plausible that SH3PXD2B might influence areal bone mineral density by regulating membrane localization and sheddase activity of MMP14. Likewise, SH3PXD2B might influence sheddase activities in other tissues as well. Given the previous demonstration of sheddase regulation by SH3PXD2A (Malinin et al. 2005), a similar function for SH3PXD2B remains possible.

Molecular biology and genetics of *Sh3pxd2b*

At the molecular level, it will be of particular importance to define additional SH3PXD2B interacting proteins. Our current experiments have been guided in two ways, previous identification of proteins interacting with SH3PXD2A/SH3PXD2B and our molecular identification of the *nee* mutation; leading to the suggestion that SH3PXD2B may interact with ADAM15. However, many additional interacting proteins likely remain to be identified. Previous studies have demonstrated interactions of SH3PXD2A with ADAM12, ADAM15, ADAM19 (Abram et al. 2003), and WASL (Oikawa et al. 2008). In addition, MMP14 (MT1-MMP) localization has previously been shown to be influenced by SH3PXD2B (Buschman et al. 2009). The possibility of interactions between SH3PXD2B and these candidates, as well as others, remain to be tested.

With a growing list of tissues displaying phenotypes associated with podosome-type adhesions, genes such as *SH3PXD2B* are attractive candidates for contributing to a number of diseases and complex traits. For example, genetic association studies for human obesity have detected suggestive linkage with *SH3PXD2B* at 5q35 (Liu et al. 2008; Zhao et al. 2007), although some studies have failed to replicate the association (Vogel et al. 2009). It is also interesting that a quantitative trait locus for growth in mice has previously been mapped near the chromosomal location of *Sh3pxd2b* (Rocha et al. 2004).

Concluding remarks

In conclusion, a phenotype-driven search for new mouse models of human disease led to identification of multiple phenotypes caused by the *Sh3pxd2b*^{nee} mutation in mice. *Sh3pxd2b* encodes a widely expressed podosomal-adaptor protein influencing postnatal growth and development of several mesenchymal derived tissues, including craniofacial structures, the ocular irideocorneal angle, and white adipose tissue. To our knowledge, this is the first report of mutant *in vivo* phenotypes associated with either *Sh3pxd2b*, or the closely related

Sh3pxd2a genes. While most studies of podosome-type adhesions to date have been dominated by studies of osteoclasts, macrophages, and tumor cells, the current findings suggest previously unknown roles for podosomes in several additional tissues. In ongoing work, it will be of particular interest to use mice with the *Sh3pxd2b*^{nee} mutation as a resource to further delineate the genetic pathways regulating function of podosome-type adhesions, to continue mechanistic studies of SH3PXD2B in specific cell-types, and to assess potential contributions of podosomal-adaptor proteins to human health and disease.

Acknowledgements

We thank Adam Hedberg-Buenz for maintaining mouse colonies at the University of Iowa; Pat Ward-Bailey for help with the *nee* mapping cross; John Fingert and Val Sheffield for contributions to DNA sequencing; Gloria Lee for kindly providing the *Src* (Y529F) construct; Michael Henry for assistance with X-ray imaging; Wayne Johnson and Robert Mullins for helpful discussions; and Michelle Curtain, an animal caretaker at The Jackson Laboratory, who observed the founder *nee* mouse and provided it to The Jackson Laboratory's Mouse Mutant Resource. We are especially grateful for many helpful discussions with Norm Hawes of The Jackson Laboratory, who recently passed away; his selfless attitude toward science and kindness were a joy and inspiration. This work was supported by EY017673 and a grant from the Knights Templar Eye Foundation, Inc. to MGA. The Mouse Mutant Resource of The Jackson Laboratory is supported by a grant from the National Center for Research Resources (RR01183); contributions to work on the craniofacial and skeletal phenotypes by LRD and BH were supported by EYO15073; contributions to the assessment of the hearing phenotype by QYZ and KRJ were supported by DC005846 and DC004301; contributions to initially recognizing ocular phenotypes of *nee* mice by BC were supported by the Foundation Fighting Blindness; and work at The Jackson Laboratory was additionally supported by National Cancer Institute Grant CA34196.

This manuscript also appears in *Mammalian Genome*. The original publication is available at www.springerlink.com

References

Abram CL, Seals DF, Pass I, Salinsky D, Maurer L, Roth TM, Courtneidge SA. The adaptor protein fish associates with members of the ADAMs family and localizes to podosomes of Src-transformed cells. J Biol Chem 2003;278:16844–16851. [PubMed: 12615925]

Acott TS, Kelley MJ. Extracellular matrix in the trabecular meshwork. Exp Eye Res 2008;86:543–561. [PubMed: 18313051]

Aga M, Bradley JM, Keller K, Kelley MJ, Acott TS. Specialized Podosome- or Invadopodia-like Structures (PILS) for Focal Trabecular Meshwork Extracellular Matrix Turnover. Invest Ophthalmol Vis Sci. 2008

Bourlier V, Zakaroff-Girard A, De Barros S, Pizzacalla C, de Saint Front VD, Lafontan M, Bouloumie A, Galitzky J. Protease inhibitor treatments reveal specific involvement of matrix metalloproteinase-9 in human adipocyte differentiation. J Pharmacol Exp Ther 2005;312:1272–1279. [PubMed: 15537822]

Buffone GJ, Darlington GJ. Isolation of DNA from biological specimens without extraction with phenol. Clin Chem 1985;31:164–165. [PubMed: 3965205]

Buschman MD, Bromann PA, Cejudo-Martin P, Wen F, Pass I, Courtneidge SA. The novel adaptor protein Tks4 (SH3PXD2B) is required for functional podosome formation. Mol Biol Cell 2009;20:1302–1311. [PubMed: 19144821]

Chang B, Hawes NL, Hurd RE, Wang J, Howell D, Davisson MT, Roderick TH, Nusinowitz S, Heckenlively JR. Mouse models of ocular diseases. Vis Neurosci 2005;22:587–593. [PubMed: 16332269]

Chen W, Yang S, Abe Y, Li M, Wang Y, Shao J, Li E, Li YP. Novel pycnodysostosis mouse model uncovers cathepsin K function as a potential regulator of osteoclast apoptosis and senescence. Hum Mol Genet 2007;16:410–423. [PubMed: 17210673]

Chun TH, Hotary KB, Sabeh F, Saltiel AR, Allen ED, Weiss SJ. A pericellular collagenase directs the 3-dimensional development of white adipose tissue. Cell 2006;125:577–591. [PubMed: 16678100]

Courtneidge SA, Azucena EF, Pass I, Seals DF, Tesfay L. The SRC substrate Tks5, podosomes (invadopodia), and cancer cell invasion. Cold Spring Harb Symp Quant Biol 2005;70:167–171. [PubMed: 16869750]

Destaing O, Sanjay A, Itzstein C, Horne WC, Toomre D, De Camilli P, Baron R. The tyrosine kinase activity of c-Src regulates actin dynamics and organization of podosomes in osteoclasts. Mol Biol Cell 2008;19:394–404. [PubMed: 17978100]

Egeblad M, Shen HC, Behonick DJ, Wilmes L, Eichten A, Korets LV, Kheradmand F, Werb Z, Coussens LM. Type I collagen is a genetic modifier of matrix metalloproteinase 2 in murine skeletal development. Dev Dyn 2007;236:1683–1693. [PubMed: 17440987]

Eto K, Huet C, Tarui T, Kupriyanov S, Liu HZ, Puzon-McLaughlin W, Zhang XP, Sheppard D, Engvall E, Takada Y. Functional classification of ADAMs based on a conserved motif for binding to integrin alpha 9beta 1: implications for sperm-egg binding and other cell interactions. J Biol Chem 2002;277:17804–17810. [PubMed: 11882657]

Evans JP. Fertilin beta and other ADAMs as integrin ligands: insights into cell adhesion and fertilization. Bioessays 2001;23:628–639. [PubMed: 11462216]

Gimona M, Buccione R. Adhesions that mediate invasion. Int J Biochem Cell Biol 2006;38:1875–1892. [PubMed: 16790362]

Gimona M, Buccione R, Courtneidge SA, Linder S. Assembly and biological role of podosomes and invadopodia. Curr Opin Cell Biol 2008;20:235–241. [PubMed: 18337078]

Green M. A rapid method for clearing and staining specimans for the demonstration of bone. The Ohio Journal of Science 1952;52:31–33.

Grisendi S, Bernardi R, Rossi M, Cheng K, Khandker L, Manova K, Pandolfi PP. Role of nucleophosmin in embryonic development and tumorigenesis. Nature 2005;437:147–153. [PubMed: 16007073]

Hikita A, Yana I, Wakeyama H, Nakamura M, Kadono Y, Oshima Y, Nakamura K, Seiki M, Tanaka S. Negative regulation of osteoclastogenesis by ectodomain shedding of receptor activator of NF-kappaB ligand. J Biol Chem 2006;281:36846–36855. [PubMed: 17018528]

Hishida T, Eguchi T, Osada S, Nishizuka M, Imagawa M. A novel gene, fad49, plays a crucial role in the immediate early stage of adipocyte differentiation via involvement in mitotic clonal expansion. Febs J 2008;275:5576–5588. [PubMed: 18959745]

Holmbeck K, Bianco P, Caterina J, Yamada S, Kromer M, Kuznetsov SA, Mankani M, Robey PG, Poole AR, Pidoux I, Ward JM, Birkedal-Hansen H. MT1-MMP-deficient mice develop dwarfism, osteopenia, arthritis, and connective tissue disease due to inadequate collagen turnover. Cell 1999;99:81–92. [PubMed: 10520996]

Kornak U, Kasper D, Bosl MR, Kaiser E, Schweizer M, Schulz A, Friedrich W, Delling G, Jentsch TJ. Loss of the ClC-7 chloride channel leads to osteopetrosis in mice and man. Cell 2001;104:205–215. [PubMed: 11207362]

Krane SM, Inada M. Matrix metalloproteinases and bone. Bone 2008;43:7–18. [PubMed: 18486584]

Linder S. The matrix corroded: podosomes and invadopodia in extracellular matrix degradation. Trends Cell Biol 2007;17:107–117. [PubMed: 17275303]

Linder S, Aepfelbacher M. Podosomes: adhesion hot-spots of invasive cells. Trends Cell Biol 2003;13:376–385. [PubMed: 12837608]

Liu YJ, Liu XG, Wang L, Dina C, Yan H, Liu JF, Levy S, Papasian CJ, Drees BM, Hamilton JJ, Meyre D, Delplanque J, Pei YF, Zhang L, Recker RR, Froguel P, Deng HW. Genome-wide association scans identified CTNNBL1 as a novel gene for obesity. Hum Mol Genet 2008;17:1803–1813. [PubMed: 18325910]

Lock P, Abram CL, Gibson T, Courtneidge SA. A new method for isolating tyrosine kinase substrates used to identify fish, an SH3 and PX domain-containing protein, and Src substrate. EMBO J 1998;17:4346–4357. [PubMed: 9687503]

Malinin NL, Wright S, Seubert P, Schenk D, Griswold-Prenner I. Amyloid-beta neurotoxicity is mediated by FISH adapter protein and ADAM12 metalloprotease activity. Proc Natl Acad Sci U S A 2005;102:3058–3063. [PubMed: 15710903]

Mosig RA, Dowling O, DiFeo A, Ramirez MC, Parker IC, Abe E, Diouri J, Aqeel AA, Wylie JD, Oblander SA, Madri J, Bianco P, Apte SS, Zaidi M, Doty SB, Majeska RJ, Schaffler MB, Martignetti JA. Loss of MMP-2 disrupts skeletal and craniofacial development and results in decreased bone mineralization, joint erosion and defects in osteoblast and osteoclast growth. Hum Mol Genet 2007;16:1113–1123. [PubMed: 17400654]

Ohbayashi N, Shibayama M, Kurotaki Y, Imanishi M, Fujimori T, Itoh N, Takada S. FGF18 is required for normal cell proliferation and differentiation during osteogenesis and chondrogenesis. Genes Dev 2002;16:870–879. [PubMed: 11937494]

Oikawa T, Itoh T, Takenawa T. Sequential signals toward podosome formation in NIH-src cells. J Cell Biol 2008;182:157–169. [PubMed: 18606851]

Ory S, Brazier H, Pawlak G, Blangy A. Rho GTPases in osteoclasts: orchestrators of podosome arrangement. Eur J Cell Biol 2008;87:469–477. [PubMed: 18436334]

Pasten-Hidalgo K, Hernandez-Rivas R, Roa-Espitia AL, Sanchez-Gutierrez M, Martinez-Perez F, Monrroy AO, Hernandez-Gonzalez EO, Mujica A. Presence, processing, and localization of mouse ADAM15 during sperm maturation and the role of its disintegrin domain during sperm-egg binding. Reproduction 2008;136:41–51. [PubMed: 18390692]

Richtsmeier JT, Baxter LL, Reeves RH. Parallels of craniofacial maldevelopment in Down syndrome and Ts65Dn mice. Dev Dyn 2000;217:137–145. [PubMed: 10706138]

Rocha JL, Eisen EJ, Van Vleck LD, Pomp D. A large-sample QTL study in mice: I. Growth. Mamm Genome 2004;15:83–99.

Saltel F, Chabadel A, Bonnelye E, Jurdic P. Actin cytoskeletal organisation in osteoclasts: a model to decipher transmigration and matrix degradation. Eur J Cell Biol 2008;87:459–468. [PubMed: 18294724]

Sharma VM, Litersky JM, Bhaskar K, Lee G. Tau impacts on growth-factor-stimulated actin remodeling. J Cell Sci 2007;120:748–757. [PubMed: 17284520]

Shi J, Son MY, Yamada S, Szabova L, Kahan S, Chrysovergis K, Wolf L, Surmak A, Holmbeck K. Membrane-type MMPs enable extracellular matrix permissiveness and mesenchymal cell proliferation during embryogenesis. Dev Biol 2008;313:196–209. [PubMed: 18022611]

Shimizu A, Maruyama T, Tamaki K, Uchida H, Asada H, Yoshimura Y. Impairment of decidualization in SRC-deficient mice. Biol Reprod 2005;73:1219–1227. [PubMed: 16107610]

Soriano P, Montgomery C, Geske R, Bradley A. Targeted disruption of the c-src proto-oncogene leads to osteopetrosis in mice. Cell 1991;64:693–702. [PubMed: 1997203]

Spinardi L, Marchisio PC. Podosomes as smart regulators of cellular adhesion. Eur J Cell Biol 2006;85:191–194. [PubMed: 16546561]

Symons M. Cell biology: watching the first steps of podosome formation. Curr Biol 2008;18:R925–R927. [PubMed: 18957242]

Tarone G, Cirillo D, Giancotti FG, Comoglio PM, Marchisio PC. Rous sarcoma virus-transformed fibroblasts adhere primarily at discrete protrusions of the ventral membrane called podosomes. Exp Cell Res 1985;159:141–157. [PubMed: 2411576]

Thompson O, Kleino I, Crimaldi L, Gimona M, Saksela K, Winder SJ. Dystroglycan, Tks5 and Src mediated assembly of podosomes in myoblasts. PLoS ONE 2008;3:e3638. [PubMed: 18982058]

Vogel CI, Greene B, Scherag A, Muller TD, Friedel S, Grallert H, Heid IM, Illig T, Wichmann HE, Schafer H, Hebebrand J, Hinney A. Non-replication of an association of CTNNBL1 polymorphisms and obesity in a population of Central European ancestry. BMC Med Genet 2009;10:14. [PubMed: 19228371]

Weaver AM. Invadopodia. Curr Biol 2008;18:R362–R364. [PubMed: 18460310]

Young JS, Guttman JA, Vaid KS, Shahinian H, Vogl AW. Cortactin (CTTN), N-WASP (WASL), and clathrin (CLTC) are present at podosome-like tubulobulbar complexes in the rat testis. Biol Reprod 2009a;80:153–161. [PubMed: 18799755]

Young JS, Guttman JA, Vaid KS, Vogl AW. Tubulobulbar complexes are intercellular podosome-like structures that internalize intact intercellular junctions during epithelial remodeling events in the rat testis. Biol Reprod 2009b;80:162–174. [PubMed: 18799754]

Zhao LJ, Xiao P, Liu YJ, Xiong DH, Shen H, Recker RR, Deng HW. A genome-wide linkage scan for quantitative trait loci underlying obesity related phenotypes in 434 Caucasian families. Hum Genet 2007;121:145–148. [PubMed: 17115187]

Zheng QY, Hardisty-Hughes R, Brown SD. Mouse models as a tool to unravel the genetic basis for human otitis media. Brain Res 2006;1091:9–15. [PubMed: 16917982]

Zheng QY, Johnson KR, Erway LC. Assessment of hearing in 80 inbred strains of mice by ABR threshold analyses. Hear Res 1999;130:94–107. [PubMed: 10320101]

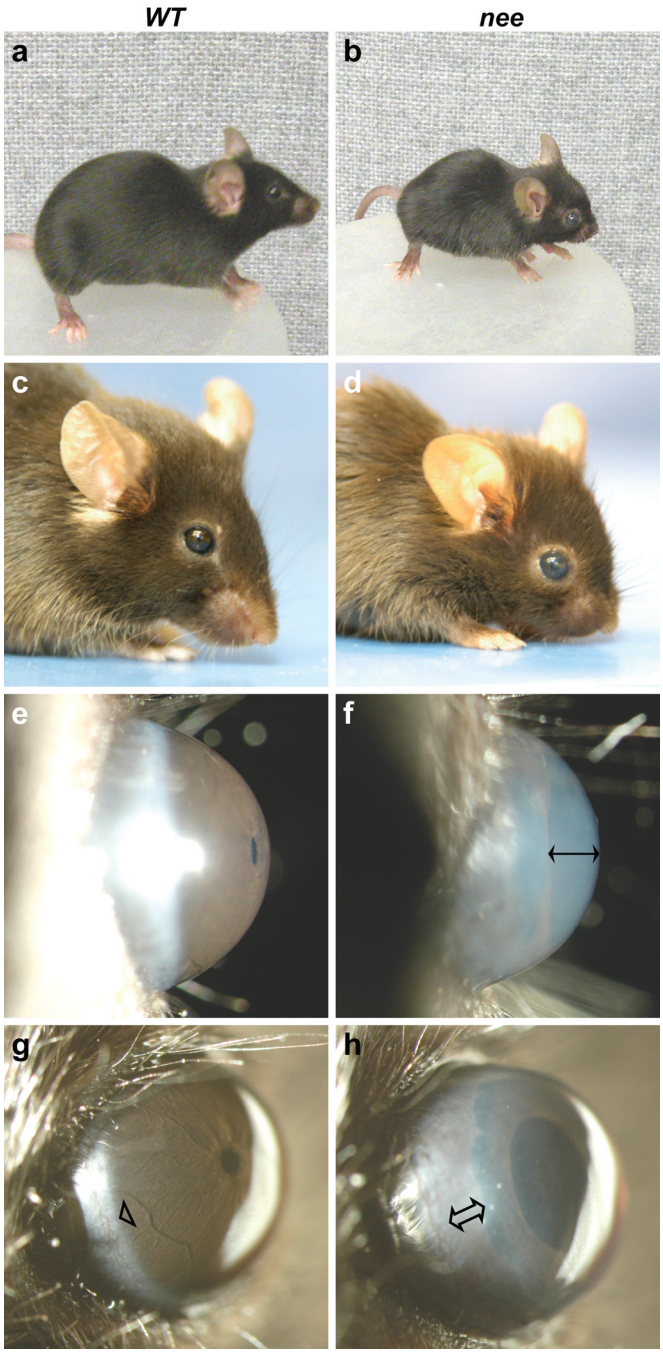

Fig. 1. Externally visible phenotypes of *nee* mice

Comparing littermate controls homozygous for wild-type alleles (*left column*) to mutant mice homozygous for the *nee* mutation (*right column*), *nee* mutants exhibit abnormal growth, craniofacial, and ocular phenotypes. **(a, b)** *nee* homozygotes exhibit small body size, as evident in this comparison of 4-month-old females. **(c, d)** Craniofacial abnormalities of *nee* homozygotes characterized by shortened noses and domed skulls. **(e–h)** Two different ophthalmic slit-lamp views of the same eyes from 1-month-old mice. Note that while wild-type mice have a clear cornea and normal anterior chamber depth (e), *nee* homozygotes have a cloudy cornea and enlarged anterior chamber (f, *black double arrow*). Viewed in this orientation, the normal mouse iris and cornea appear very close to one another, leaving little

to no discernable depth to the anterior chamber. The irideocorneal angle of wild-type mice is characterized by a sharply defined limbus (g, *arrowhead*), whereas the irideocorneal angle of *nee* homozygotes has severe peripheral anterior synechia (h, *double arrow*).

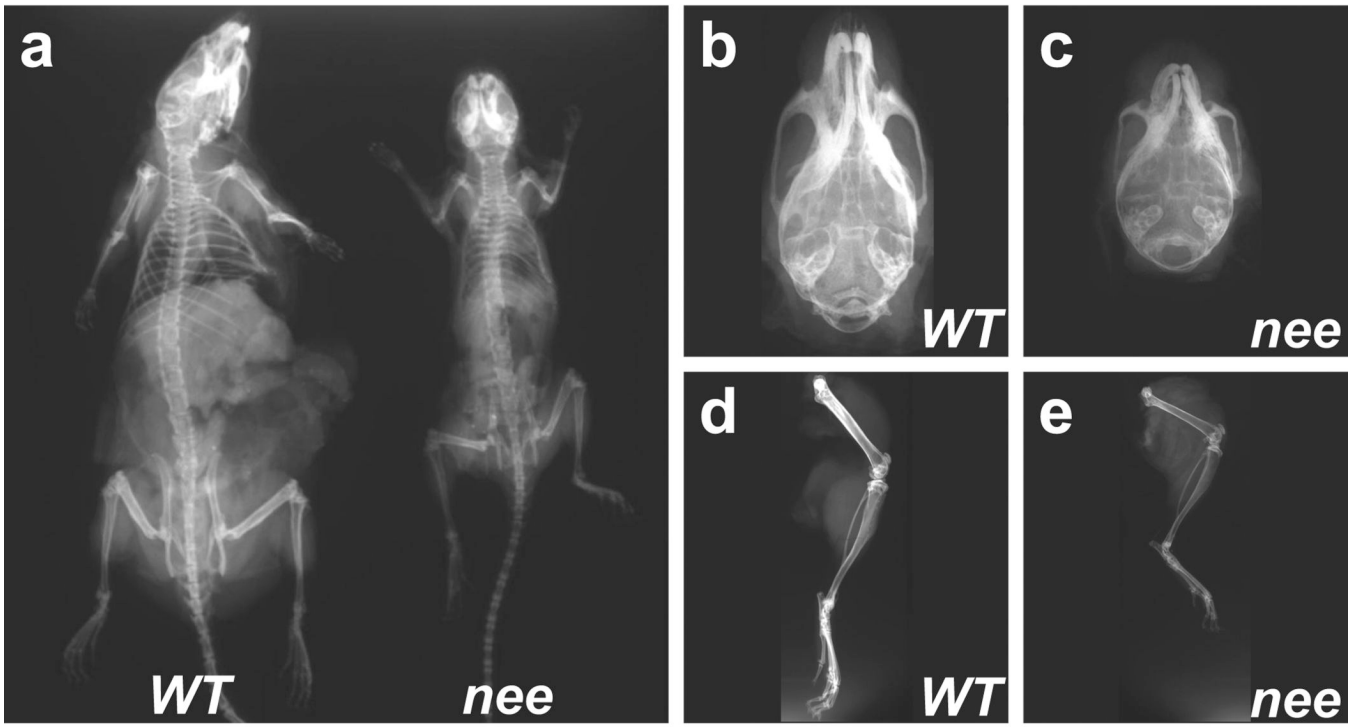

Fig. 2. Skeletal defects of *nee* mice

X-ray imaging of mutant *nee* mice and wild-type littermate controls indicates the presence of multiple skeletal abnormalities in *nee* homozygotes. **(a)** Adult *nee* homozygotes have a proportionally smaller skeleton in comparison to wild-type littermate controls. **(b, c)** Higher magnification dorsal views of skulls showing a drastically reduced anterior-posterior length and slightly reduced width in *nee* homozygotes. **(d, e)** Higher magnification view showing that hind legs of *nee* homozygotes are reduced in size, but otherwise largely normal in anatomical appearance. Images from the same pair of 12-month-old female mice; littermate control is homozygous for the wild-type allele.

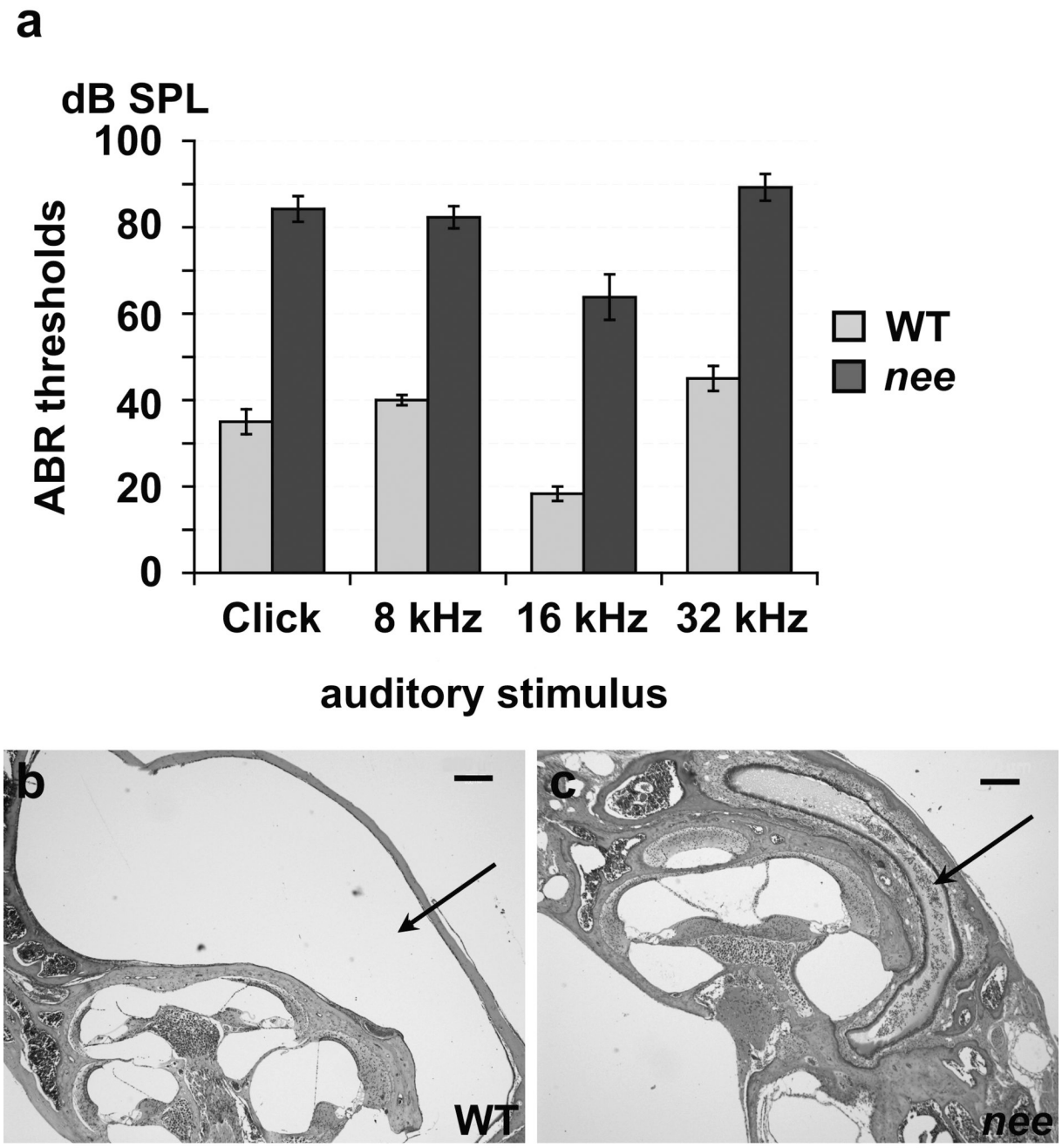

Fig. 3. Hearing impairment and ear pathology associated with the *nee* mutation

Physiologic and histologic analyses demonstrate a hearing deficiency in *nee* homozygotes associated with inflammation of the middle ear (otitis media). **(a)** ABR thresholds in response to different auditory stimuli, comparing 13 mice homozygous for the *nee* mutation to 3 heterozygous controls. Mean ABR thresholds (dB SPL) ± SEM. All mice were tested at 34–92 days of age. **(b)** Histological section of inner and middle ear from a heterozygous control showing normal anatomy and absence of cellular infiltrate in the middle ear (*arrow*). **(c)** Histological section of inner and middle ear from *nee* homozygote showing inflammation indicated by the presence of neutrophils in the middle ear cavity (*arrow*) and thickened surrounding epithelium. All inner ear structures are normal in appearance. The apparent

different size of the middle ear cavity between panels b and c is an artifactual consequence of slightly different planes of section. Scale bar = 200 μm.

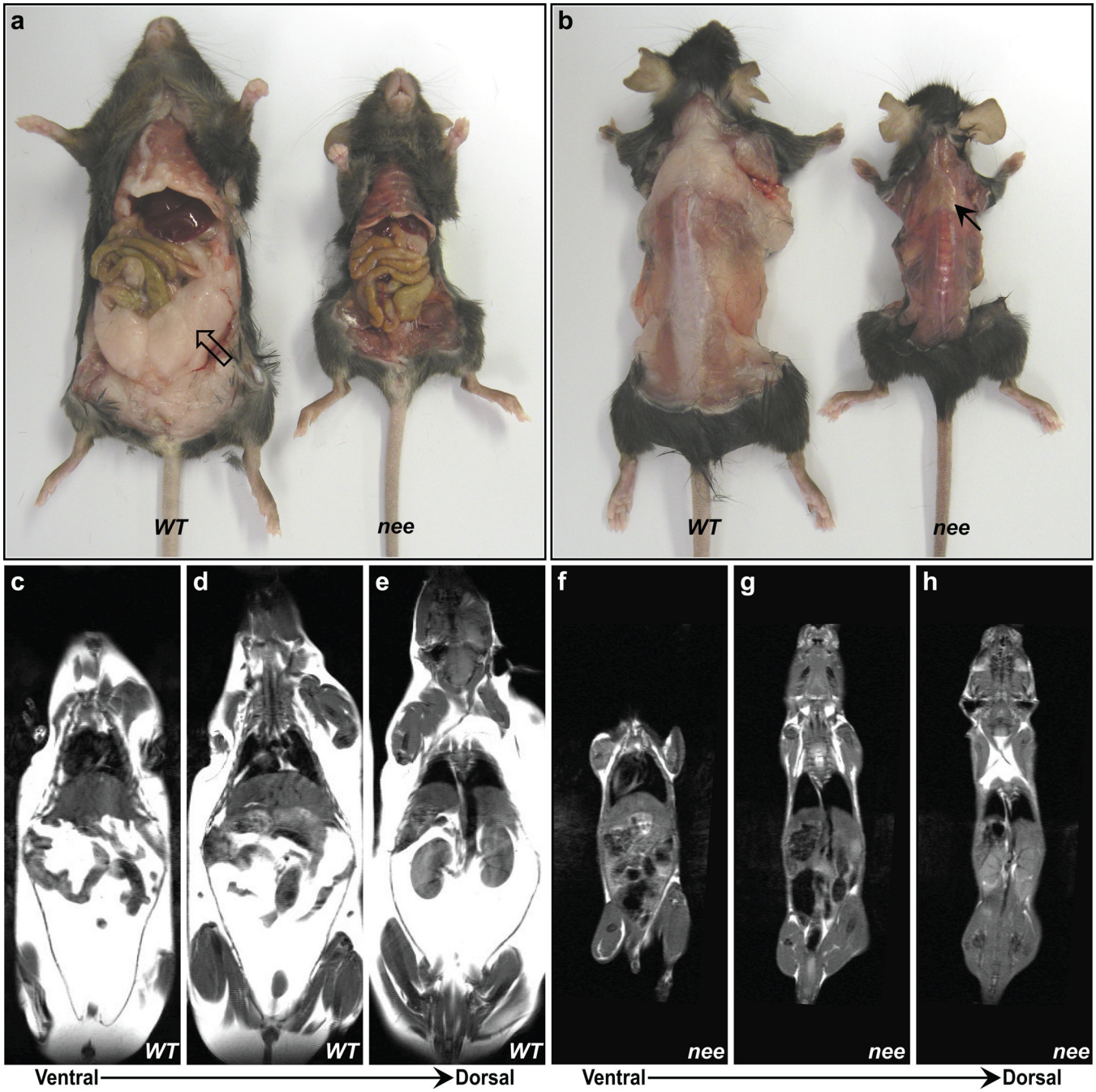

Fig. 4. Adipose defects of *nee* mice

Dissections and MRI analysis of mutant *nee* mice and wild-type littermate controls show that mice homozygous for the *nee* mutation develop a form of lipodystrophy. **(a)** Ventral and **(b)** dorsal views of wild-type littermate and *nee* homozygote. As observed in perigenital fat (*open arrow*), *nee* homozygotes show a severe depletion of white adipose tissue. In contrast, as observed in interscapular fat (*black arrow*), brown adipose tissue is maintained. **(c–h)** Coronal slices obtained by MRI showing an absence of subcutaneous and visceral adipose tissue in *nee* homozygotes. With this pulse-sequence, fat appears white and muscle and water appear gray or black. Images from the same pair of 8-month-old female mice; littermate control is homozygous for the wild-type allele.

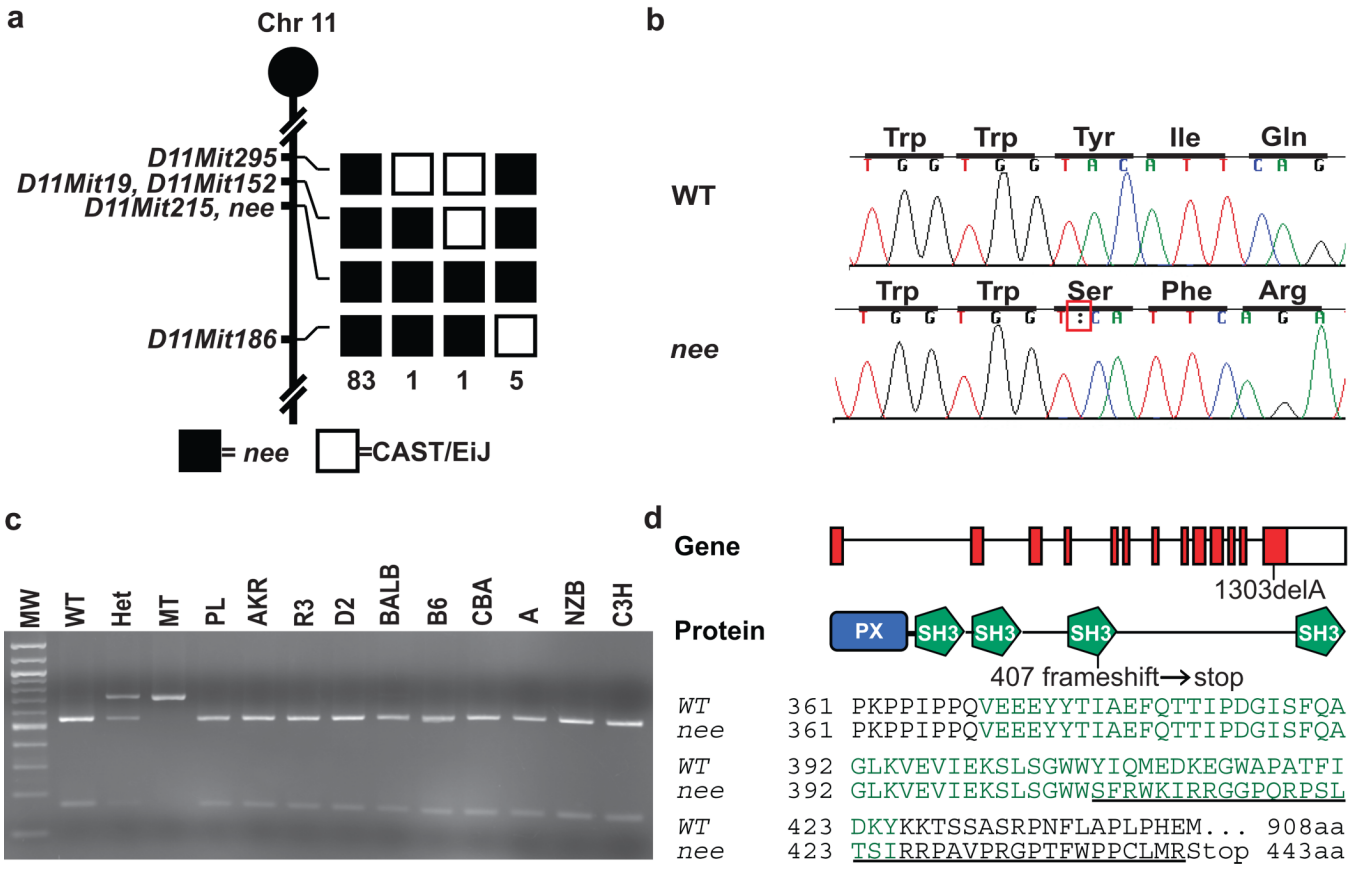

Fig. 5. Molecular identification of the *nee* mutation

(a) Genetic mapping of the *nee* mutation. Haplotype analyses of 45 mice from an intersubspecific intercross between *nee* and CAST/EiJ mice (*filled boxes*, *nee* allele; *open boxes*, CAST/EiJ allele). The number of chromosomes with each haplotype is indicated below each column. Linkage to several markers on mouse Chr 11 was observed with no recombination with *D11Mit 215*. **(b)** DNA sequence identifying a 1 bp deletion in *Sh3pxd2b*. **(c)** Restriction enzyme analysis of *nee* spanning amplicons from a wild-type littermate, *nee* heterozygote, *nee* homozygote, and 10 different inbred strains not exhibiting the *nee* phenotype. Only DNA from mice with the *nee* allele failed to be digested, indicating that the 1 bp deletion of *nee* is unique to this strain (WT, parental wild-type strain; Het, *nee* littermate heterozygous for wild-type and *nee* alleles; MT, mutant *nee* homozygote; PL, PL/J; AKR, AKR/J; R3, RIIIS/J; D2, DBA/2J; BALB, BALB/cJ; B6, C57BL/6J; CBA, CBA/J; A, A/J; NZB, NZB/BlNJ; C3H, C3H/HeJ). **(d)** Schematic of *Sh3pxd2b* gene, predicted proteins domains, and location of *nee* mutation. *Top*, the *nee* mutation (1303delA) is predicted to result in a frameshift starting at amino acid 407 altering 37 amino acids before causing a premature stop codon (*boxes*, exons; *red*, coding sequence; *blue*, PX domain; *green*, SH3 domains). *Bottom*, these changes are predicted to alter a portion of the third and entirely delete the fourth SH3 domains (*green text*, third SH3 domain; *underlined text*, frameshift).

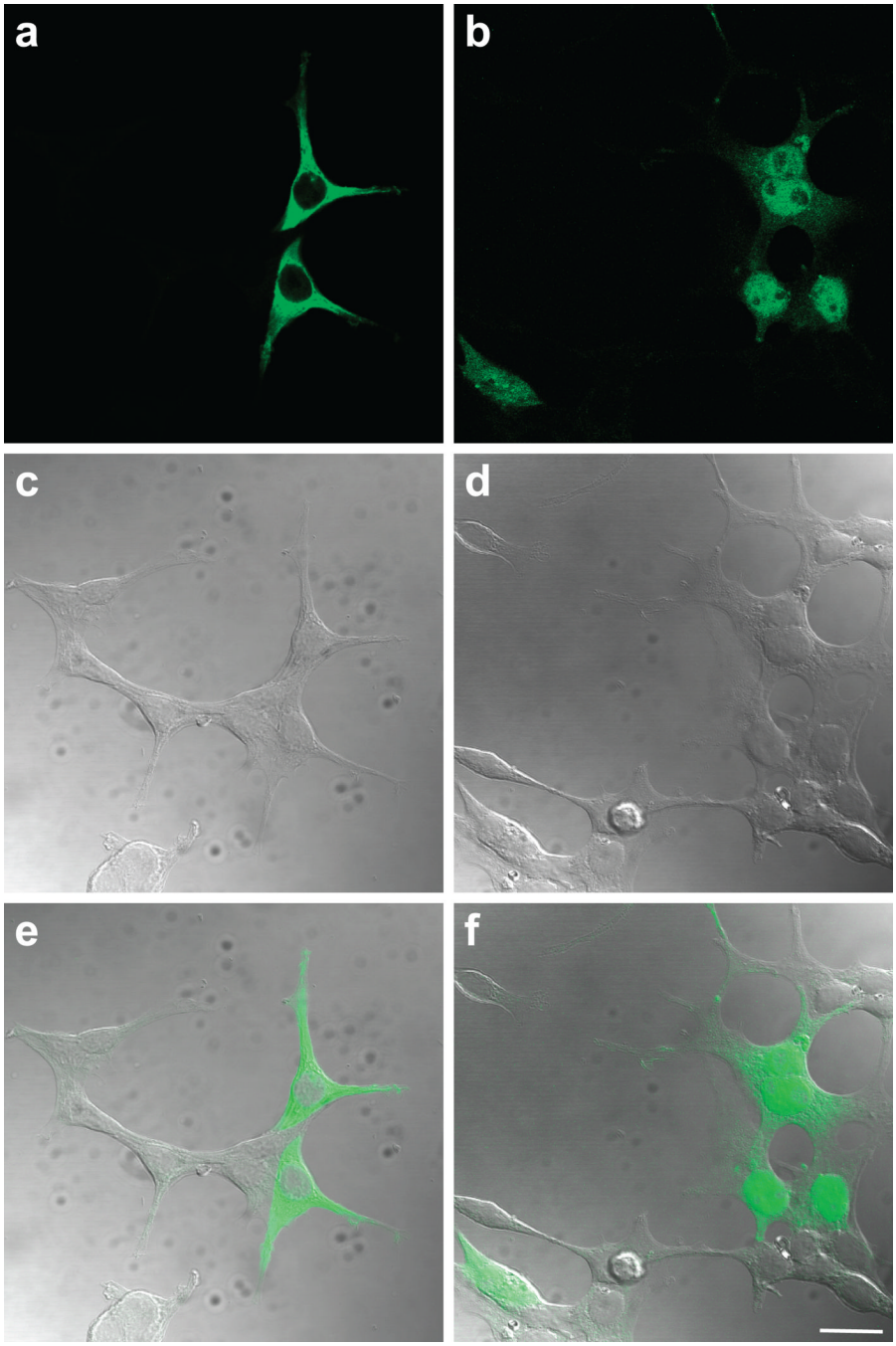

Fig. 6. Altered subcellular distribution of SH3PXD2B^{1303delA}

HEK 293T cells transfected with GFP-fusion vectors show that the 1303delA deletion alters subcellular localization of SH3PXD2B (*left column*, GFP-SH3PXD2B; *right column*, GFP-SH3PXD2B^{1303delA}). **(a)** GFP fluorescence is present in the cytoplasm but not in the nucleus of cells transfected with GFP-tagged wild-type SH3PXD2B. (**b**) GFP-tagged mutant protein is present throughout the cell, including prominent localization within the nucleus. **(c, d)** Phase-contrast and **(e, f)** merged images of the same fields. Images were collected with a 63X objective; scale bar = 20 μm.

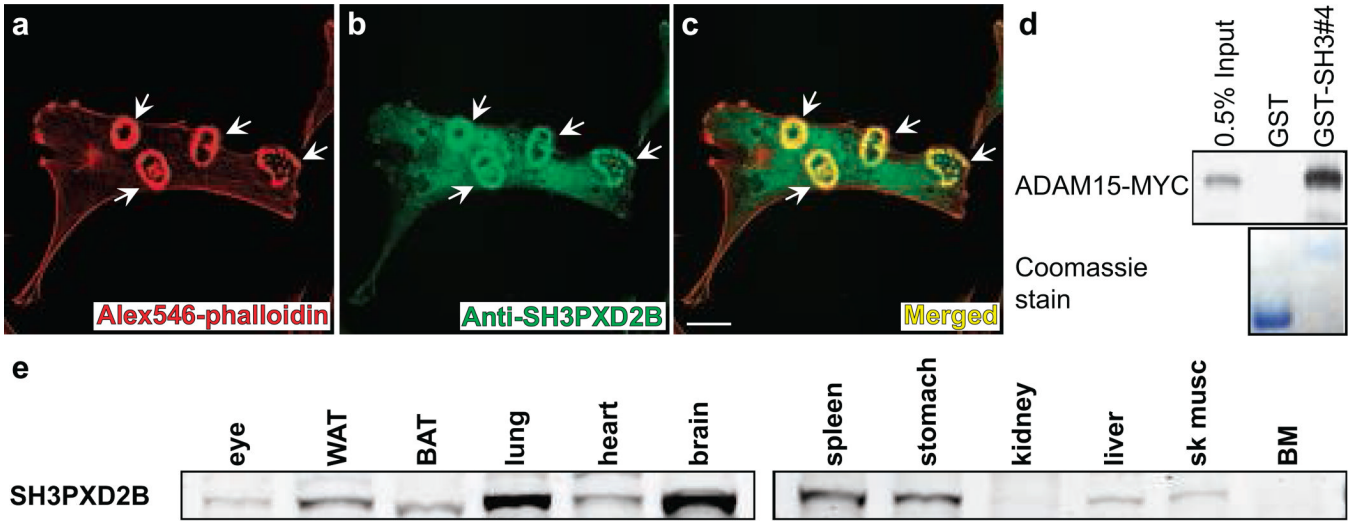

Fig. 7. Localization, protein interaction, and tissue distribution of SH3PXD2B

(a–c) NIH3T3 cells transiently transfected with constitutively active *Src* (Y529F) contain SH3PXD2B localized to clusters and rosettes of podosomes (*white arrows*, podosomes; *red*, F-actin; *green*, SH3PXD2B; *yellow*, merge). Images were collected with a 63X objective; scale bar = 20 μm **(d)** GST pull-down experiment indicating association between SH3PXD2B and ADAM15. Protein content is evident by the coomassie blue stained SDS-PAGE gel indicating presence of 26 kDa GST and 34 kDa GST-SH3#4. **(e)** Western blot showing that SH3PXD2B has a broad, but not ubiquitous, tissue distribution (WAT, perigenital white adipose tissue; BAT, interscapular brown adipose tissue; sk musc, skeletal muscle; BM, bone marrow).